# Liquid–Liquid Phase Transition in Nanoconfined Silicon Carbide

Weikang Wu,[†] Leining Zhang,[†] Sida Liu,[†] Hongru Ren,[†] Xuyan Zhou,[†] and Hui Li*,[†]

[†]Key Laboratory for Liquid–Solid Structural Evolution and Processing of Materials, Ministry of Education, Shandong University, Jinan 250061, People's Republic of China

ABSTRACT: We report theoretical evidence of a liquid–liquid phase transition (LLPT) in liquid silicon carbide under nanoslit confinement. The LLPT is characterized by layering transitions induced by confinement and pressure, accompanying the rapid change in density. During the layering transition, the proportional distribution of tetracoordinated and pentacoordinated structures exhibits remarkable change. The tricoordinated structures lead to the microphase separation between silicon (with the dominant tricoordinated, tetracoordinated, and pentacoordinated structures) and carbon (with the dominant tricoordinated structures) in the layer close to the walls. A strong layer separation between silicon atoms and carbon atoms is induced by strong wall–liquid forces. Importantly, the pressure confinement phase diagram with negative slopes for LLPT lines indicates that, under high pressure, the LLPT is mainly confinement-induced, but under low pressure, it becomes dominantly pressure-induced.
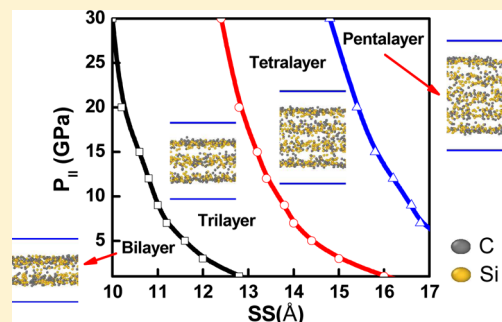
■ INTRODUCTION

Silicon, especially its crystalline and amorphous forms, remains one of the most important technological materials because of its wide applications in solid-state electronics and photovoltaic technologies. Remarkably similar to water,[1,2] glassy silicon has been found to have interesting polyamorphism characterized by discontinuous structural (or volumetric) changes. For example, McMillan et al.[3–6] adopted the X-ray diffraction and Raman spectroscopy measurements, as well as MD simulations to observe a density-driven phase transition from the high-density amorphous (HDA) form to low-density amorphous (LDA) silicon upon decompression. McMillan et al.'s work[3,4] links the amorphous polyamorphism to critical fluctuations related to an underlying liquid–liquid phase transition (LLPT) in super-cooled silicon, as originally predicted by Aptekar.[7] Sastry and Angell presented theoretical evidence using the Stillinger–Weber potential to support a first-order transition from a high-density liquid (HDL) to a low-density liquid (LDL) in the supercooled silicon at $T \approx 1060$ K (at zero pressure),[8] supported by subsequent experimental and simulation studies.[9–13] The coexistence of two completely different bonding species in liquid silicon, metallic and covalent, is believed to be a precondition for the LLPT.[7,14] The metallic bond nature favoring the isotropic symmetry would increase the density, while the covalent bond favoring the tetrahedral symmetry facilitates the lower density of LDL.[15] On this account, the LDL is nearly tetracoordinated with diamond-type structures, while the HDL is more highly coordinated and white-tin-like in nature.[10,13,16,17] The structural nature of the LDL and HDL determined by bonding species is consistent with the tetrahedrally bonded LDA with semiconductor features and the highly coordinated metallic HDA confirmed in refs 4 and 5. According to extensive numerical simulations,[10,18–20] based on

the extrapolation of the LDA–HDA transition line,[3–5] the LDL and HDL in supercooled silicon are also separated by a line of first-order transition which, however, ends at a critical point with negative pressures in the temperature–pressure plane. Moreover, the LLPT in supercooled silicon was found to be accompanied by the anomalous change in diffusivity[21] and a fragile to strong transition.[8,22,23] Consequently, due to the rich and intriguing structural behavior in the liquid silicon, there has been tremendous interest in the LLPT in supercooled silicon as well as other systems that form a tetrahedrally coordinated network.

Similar to silicon, carbon has also been suggested for the possibility of an LLPT.[24–31] The LLPT in liquid carbon was believed to occur at the known maximum in the melting line of graphite,[24,26] as a consequence of constraints on the strain energy between graphitic and diamond-like liquid clusters.[25] Stimulated by Togaya's indirect evidence[27] for the LLPT through a flash-heating experiment under high pressure, Glosli and Ree[28] suggested a transition between a predominantly sp-bonded (with little sp[3] character) LDL and a mostly sp[3]-bonded (little sp character) HDL with a critical point at 8801 K and 10.56 GPa, by means of classical molecular dynamics (MD) calculations with Brenner's bond-order potential. However, a first-principles investigation[32] ruled out the occurrence of such a transition at 6000 K. Subsequent theoretical simulations[29,33,34] also did not confirm the occurrence of an LLPT in carbon. Even so, the structural change in liquid carbon with respect to temperature and pressure cannot be ignored.[29,30,32,35] For instance, Wu et al.[32] pointed out a continuous transformation from a sp/sp²-like liquid to a sp²/sp³

liquid as a function of pressure, above the graphite melting line. Furthermore, Correa et al.[36] also found a maximum in the pressure−temperature melting line of diamond, indicating a potential LLPT in the diamond range. Although diamond was found to undergo metalization upon melting,[36,37] no sign of an LLPT near the maximum point is found.[38,39] Above all, there is still no unanimous view about the existence of LLPT in carbon, and much effort should be devoted to studying the liquid carbon structure.

Potential LLPTs in both liquid silicon and carbon raise an interesting question about the existence of an LLPT in the liquid silicon carbide (SiC). Novel LLPT characteristics should be found when the high-coordinated silicon atoms mix with the low-coordinated carbon atoms, but the study of the LLPT in liquid SiC is currently lacking. Silicon carbide is one of the most promising materials for power electronics, hard materials, and biomaterials, due to its superior properties.[40] Specifically, 2D-SiC is reported to have a moderate direct band gap[41,42] and exhibits improved photoluminescence capability.[43] Confining liquid in quasi-one or two dimensions is believed to lead to the discovery of new and controversial phenomena in experiments and simulations[44−46] and is also a powerful way of synthesizing nanomaterials in a controlled manner.[47,48] In the present work, we confine the liquid SiC between two infinite parallel walls and have observed layering transitions controlled by slit sizes. Layered structures have been acquired and investigated in several physical and chemical systems, such as ionic liquids.[49,50] Here, we consider that the layering transition is actually a type of LLPT. This work would provide the theoretical evidence of the existence of the LLPT in the confined liquid SiC and have a guiding significance in the fabrication of 2D-SiC.

■ MODELS AND THEORETICAL METHODS

We perform the simulation using the software package LAMMPS.[51] The liquid is composed of 2700 silicon atoms and 2700 carbon atoms. The pair interaction between particles is modeled with the bond-order Tersoff potential,[52] which can consider covalent bonds forming/breaking and has shown great success in simulating the melting property of various SiC structures.[53,54] Wall−liquid interactions are represented by 6−12 Lennard-Jones (LJ) potentials with the following parameters:[55,56] $\varepsilon_{Si-wall} = 0.008909$ eV, $\varepsilon_{C-wall} = 0.002844$ eV, $\sigma_{Si-wall} = 3.629$ Å, and $\sigma_{C-wall} = 3.400$ Å. The normal of the walls is in the z direction. Periodic boundary conditions are applied along the directions x and y.

All simulations are carried out using the NPT ensemble. The Nosé−Hoover thermostat and barostat are adopted to control temperature and pressure, respectively, and the velocity−verlet algorithm is used to integrate the equation of motions with a time step of 1 fs. We exert the constant pressure parallel to walls ($P_∥$) and calculate the pressure perpendicular to walls ($P_⊥$). $P_⊥$ is obtained as the total force exerted by particles on each wall divided by wall areas. In the z direction, the slit size (SS) ranges from 10 to 17 Å. After equilibrating the system at $T = 6000$ K for 500 ps, we cool the system to the target temperature of $T = 3200$ K with a cooling rate of 1 K/ps. Final structures are obtained after relaxation for 3000 ps at $T = 3200$ K, where systems reach equilibration in approximate 1000 ps. We repeat the simulation at different $P_∥$ ranging from 1 to 30 GPa. The structural evolution at different wall−liquid LJ epsilon parameters is also investigated.

■ RESULTS AND DISCUSSION

We plot the density profile [$\rho_a(z)$] of the nanoconfined liquid SiC along the z direction at different pressure and slit sizes in Figure 1, which is measured by calculating the atomic number density within a thin slice with the thickness of 0.05 Å in the z
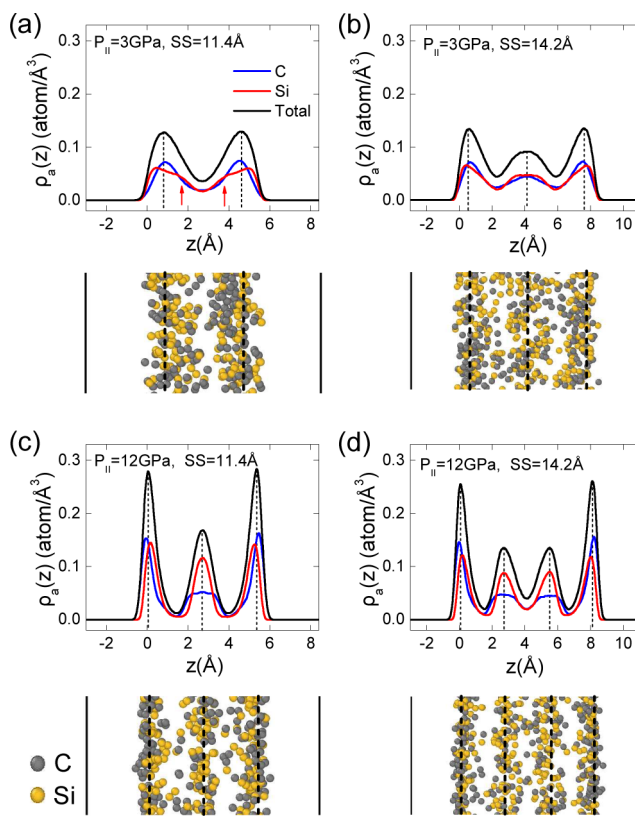
Figure 1. Density profiles [$\rho_a(z)$] and snapshots of the nanoconfined silicon carbide liquid at (a) $P_∥ = 3$ GPa, SS = 11.4 Å; (b) $P_∥ = 3$ GPa, SS = 14.2 Å; (c) $P_∥ = 12$ GPa, SS = 11.4 Å; (d) $P_∥ = 12$ GPa, SS = 14.2 Å. In the snapshot, the dashed line shows the location of layers, while walls are marked by solid lines. The peak in density profiles indicates layers. As the slit size increases from 11.4 to 14.2 Å, the structure changes from bilayer to trilayer at $P_∥ = 3$ GPa and from trilayer to tetralayer at $P_∥ = 12$ GPa. As pressure increases from 3 to 12 GPa, the structure changes from bilayer to trilayer at SS = 11.4 Å and from trilayer to tetralayer at SS = 14.2 Å. The red arrow in (a) indicates the peak shoulder of the density profile of silicon.

direction. At $P_∥ = 3$ GPa, we observe a transition from the bilayer liquid (BIL) at SS = 11.4 Å to the trilayer liquid (TRIL) at SS = 14.2 Å as indicated by snapshots and the peaks of $\rho_a(z)$. At SS = 11.4 Å, a BIL−TRIL transition is also observed as $P_∥$ increases from 3 to 12 GPa. We consider the BIL−TRIL transition as an LLPT since the layering liquid is the stable equilibrium state at a specific slit size and pressure. In comparison with the transition controlled by the slit size, high pressure makes the confined liquid more ordered and denser, inducing a more obvious layering phenomenon. Silicon and carbon show different features during the LLPT: the density profile of silicon shows more obvious inner peaks than carbon, especially under higher pressure, where the inner peak of carbon is quite chunky, as presented in Figure 1c,d; the carbon atom seems to be more tightly adsorbed on walls than silicon atoms at $P_∥ = 12$ GPa, contrary to that at $P_∥ = 3$ GPa. Besides, there are inside peak shoulders (indicating sublayers) in the density profile of silicon in the BIL, as shown in Figure 1a.

To further clarify the LLPT, we investigate the evolution of atomic structures and bonds in liquid SiC. Silicon shows more various bond types than carbon. We find that the main coordination number of silicon is 3, 4, and 5 (different from pure liquid silicon[57]), while carbon has the dominant
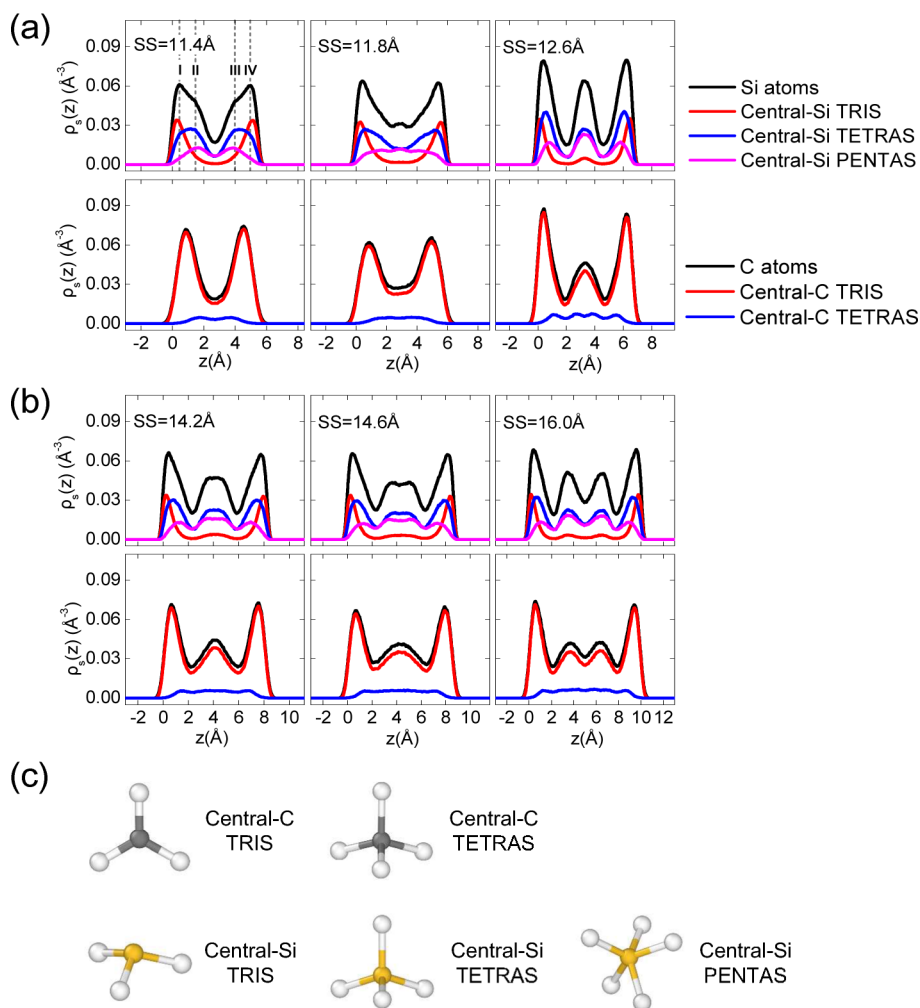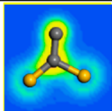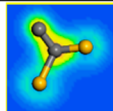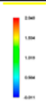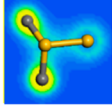
Figure 2. Number density profiles $[\rho_s(z)]$ of different coordinated structures at $P_\parallel$ = 3 GPa. (a) System changes from bilayer to trilayer, as slit sizes increase from 11.4 to 12.6 Å. (b) System changes from trilayer to tetralayer, as slit sizes increase from 14.2 to 16.0 Å. The top row in (a) and (b) represents the evolution for the tricoordinated (TRIS, red), tetracoordinated (TETRAS, blue), and pentacoordinated (PENTAS, magenta) structures of silicon, while the bottom row represents the evolution for the tricoordinated (TRIS, red) and tetracoordinated (TETRAS, blue) structures of carbon. The density profiles (black lines) of silicon atoms and carbon atoms in the confined system are also present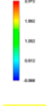ed for comparison. The dashed line in (a) at SS = 11.4 Å reveals the sublayers I, II, III, and IV of silicon in liquid SiC. (c) Different coordinated structures. Specifically, the central-C TRIS has a planar structure, showing the sp^2 characteristic of carbon atoms; the structure of central-Si TRIS is a quadrihedron.

tricoordinated structure (TRIS). The coordination number is determined by the Tersoff potential parameters:[52] cutoff$_{Si-Si}$ = 3.00 Å, cutoff$_{Si-C}$ = 2.51 Å, and cutoff$_{C-C}$ = 2.10 Å; the configurations of TRIS, tetracoordinated structures (TETRAS), and pentacoordinated structures (PENTAS) are shown in Figure 2c. Notably, the TRIS of carbon in our system tends to form a planar structure, exhibiting the sp^2 characteristic, while the structure of central-Si TRIS is a quadrihedron that can be seen as an incomplete TETRAS to lose an atom. Such a difference leads to the different structural evolution between carbon atoms and silicon atoms during LLPTs. Table 1 shows the electron density distribution of several typical dominant coordinated structures calculated by CASTEP.[58] Electrons mainly shift to carbon atoms, indicating a relatively strong bonding between carbon atoms and silicon atoms. Figure 2 presents the number density profiles $[\rho_s(z)]$ of different coordinated structures at $P_\parallel$ = 3 GPa, which is measured by counting the atom with different coordination number inside a thin slice with the thickness of 0.05 Å in the z direction. For comparison, the density profiles of silicon atoms and carbon

atoms in the confined system are also presented. At SS = 11.4 Å, the inner sublayers of silicon in the BIL is mainly determined by the TETRAS and PENTAS while the sublayer I and IV consist of TETRAS and TRIS, as shown in Figure 2a. The density profile of silicon's TETRAS shows subpeaks, and the PENTAS occupies the sublayer II and III at the same time. The PENTAS only holds a large proportion distant from walls, similar to Wilson et al.'s work,[59] where five-coordinate sites increase in comparison with the Si136/liquid interface and the diamond/liquid interface. For the central-C TRIS, which tends to form planar structures, the optimal position is adjacent and parallel to walls, leading to the quite chunky inner peak in carbon's density profiles. Although the TRIS of silicon likes to be close to walls, the TETRAS-like structure makes it less challenging than the central-C TRIS when orienting along walls, which indicates that the wall absorption of carbon atoms is tighter than that of silicon atoms at high pressure. During the LLPT from BIL to TRIL, the inner sublayers for the central-Si TETRAS gradually disappear, followed by the appearance of the middle peak; more PENTAS of silicon appears in the new

Table 1. Electron Density Distribution Slice Map of Dominant Coordinated Structures

Structure	Bilayer phase	Trilayer phase	Electron density $(e/Å^3)$
Central-C TRIS			
Central-Si TRIS			
Central-Si TETRAS			
Central-Si PENTAS			
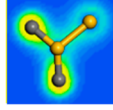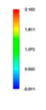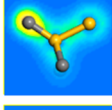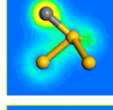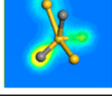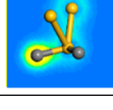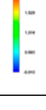
middle layer; the TRIS of both silicon and carbon mainly occupy the layer adjacent to walls. Thus, the confinement greatly affects the distribution of coordinated structures, and silicon shows more complex features than carbon due to the reverse bond structures. For the LLPT from the TRIL to the tetralayer liquid (TETRAL) in Figure 2b, the inner peak gradually splits into two subpeaks, but the TRIS is still concentrated adjacent to the walls. It can be concluded that the differences between silicon and carbon in the confined liquid SiC during LLPTs are mainly determined by the distribution of their dominant coordinated structures.

To explore the microscopic details within layers in the liquid SiC, the atomic arrangements in the layer of TRIL are presented in the Figure 3. We divide the confined space into
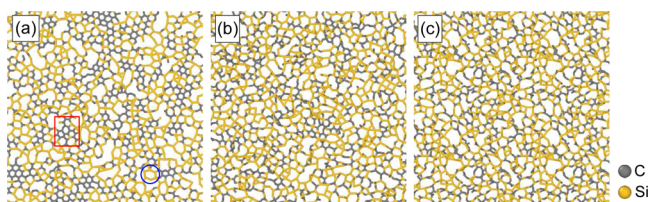

Figure 3. (a,b) Snapshot of a trilayer system at $P_∥$ = 3 GPa, SS = 14.2 Å. Atoms are located in (a) a slab next to one wall (−0.57 Å ≤ z ≤ 2.25 Å) and (b) at the central slab (2.25 Å ≤ z ≤ 5.90 Å). (c) Snapshot of a slab with a width of 3.65 Å in the free liquid under P = 3 GPa. Carbon atoms in the layer next to walls tend to gather together, forming hexagonal networks (red rectangular), while there are only few hexagonal structures (blue circle) composed by silicon atoms.

three slabs: the slabs next to two walls (z ≤ 2.25 Å and z ≥ 5.90 Å) and the central slab (2.25 Å ≤ z ≤ 5.90 Å). These definitions are based on the location of the minima in $\rho_a(z)$ observed at $P_∥$ = 3 GPa, SS = 14.2 Å (Figure 1b); such minima are at z = 2.25 and 5.90 Å. The atomic configurations of the slab next to one of the walls and the central slab are presented in Figure 3a,b, respectively. Figure 3c shows the atomic arrangement in the free liquid SiC at P = 3 GPa, which is selected from a slab with the width of 3.65 Å in accordance with

the central slab width in the TRIL. In the slab adjacent to the walls, the carbon atoms and silicon atoms show separation features. Carbon atoms tend to gather together and form hexagonal networks on the basis of the dominant TRIS, which should be attributed to the reduction of interface energy between the carbon network and the liquid environment caused by the wall effect. Notably, the holes existing around the carbon networks reveal the mismatch between the networks and the surrounding environment. The silicon atoms with dominant TRIS and TETRAS in the layer next to walls exhibit disordered features with few hexagonal structures but fail to form hexagonal networks due to the nonplanar structure of TRIS and TETRAS. Figure 3a shows a slight wall-induced micro-phase separation between carbon atoms and silicon atoms in our system, indicating the possibility of macroscopic phase separation in liquid SiC. Chehaidar et al.[60] found two peaks for Si−Si and C−C bonds in the Raman spectroscopy of amorphous SiC, suggesting that a local phase separation should be considered.[40] Therefore, the phase separation might be foreseen in the macroscopic "real" liquid SiC. The atomic configuration in the central slab seems much closer to the free liquid, where silicon atoms and carbon atoms mix quite well. To conclude, the wall confinement would bring about the heterogeneous distribution of TRIS adjacent to walls but fail to affect the configuration of central layers.

Figure 4a visualizes the density evolution of the confined liquid at $P_∥$ = 1, 3, and 12 GPa, as slit sizes increase from 10 to
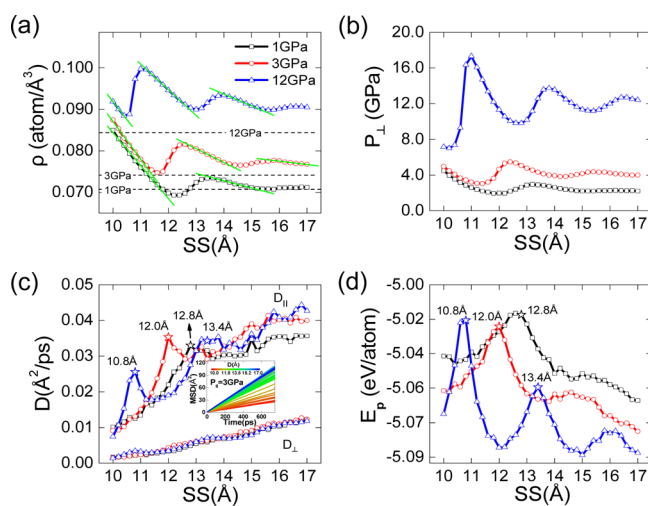
Figure 4. (a) Density (ρ) of the system, (b) pressure perpendicular to walls ($P_⊥$), (c) diffusion coefficient parallel to walls ($D_∥$) and perpendicular to walls ($D_⊥$), and (d) average potential energy (E_p) as a function of slit sizes for three different pressures of 1 GPa (square), 3 GPa (circle), and 12 GPa (top triangle). The densities of free silicon carbide liquid are shown as the dashed lines in (a). The top three curves in (c) show the change of $D_∥$, and the bottom three curves show the change of $D_⊥$. The mean square displacement curves [the inset in (c)] show that the system should be characterized as a liquid. The peak positions of $D_∥$ in (c) are in agreement with those of E_p in (d), as characterized by stars.

17 Å. The density can be seen as the average of the total density profile in Figure 1. For each $P_∥$, the density exhibits fluctuation with respect to slit sizes. At $P_∥$ = 3 GPa, for instance, we can divide the density curve into five regions: three regions with linear decrease (SS = 10−11.6 Å, SS = 12.6−14.6 Å, and SS = 15.8−17 Å) and two regions with rapid increase (SS = 11.6−

12.6 Å and SS = 14.6−15.8 Å). For the region with linear decrease, the system is in the state of the BIL, the TRIL, and the TETRAL, respectively, as the slit size increases. Thus, during the first rapid increase of density over SS = 11.6−12.6 Å, the system changes from the BIL to the TRIL, while a TRIL−TETRAL transition is exhibited when the slit size increases from 14.6 to 15.8 Å. The BIL−TRIL transition and the TRIL−TERTAL transition should be seen as LLPTs, based on the definition of the LLPT, which is characterized by the rapid change of density.[61] The increase of density in the BIL−TRIL transition (ρ = 0.07474−0.08151 atom/Å^3) is larger than that in the TRIL−TERTAL transition (ρ = 0.07648−0.07764 atom/Å^3), which indicates the weakening of the nanoconfinement effect as the slit size increases. The LLPT between different liquid layering phases is also found under $P_{\parallel}$ = 1 and 12 GPa, as presented in Figure 4a. Besides, the LLPT occurs in smaller slit sizes under higher $P_{\parallel}$. For example, at $P_{\parallel}$ = 12 GPa, the BIL−TRIL LLPT can be found over SS = 10.4−11.2 Å, prior to that (SS = 11.6−12.6 Å) at $P_{\parallel}$ = 3 GPa, which suggests that the LLPT and the liquid state are determined by $P_{\parallel}$ and slit sizes cooperatively. Upon $P_{\parallel}$ increasing, the confined liquid shows density increases and gradually becomes denser than the free liquid. For the confined liquid characterized by layers, generally $P_{\perp} \neq P_{\parallel}$, contrary to the homogeneous free liquid. Figure 4b shows that, similar to the evolution of density at a constant $P_{\parallel}$, with the increase of the slit size, $P_{\perp}$ decreases in the stage of the BIL, TRIL, and TETRAL but shows rapid increases during LLPTs. This should be reasonable because the appearance of a new layer during the BIL−TRIL and TRIL−TETRAL transition would increase the pressure perpendicular to walls.

We calculated the diffusion coefficient by measuring the mean square displacement curve. Since the z direction is confined by walls, we consider the diffusivity in the x−y plane and in the z direction. As shown in Figure 4c, at each $P_{\parallel}$, $D_{\parallel}$ is much larger than $D_{\perp}$, showing the strong confinement effect. Both $D_{\parallel}$ and $D_{\perp}$ show an increasing trend as the slit size increases from 10 to 17 Å, indicating that the atomic activity strengthens because the confinement effect weakens. In comparison with the monotonic increase of $D_{\perp}$, $D_{\parallel}$ shows peaks at ($P_{\parallel}$, SS) = (1 GPa, 12.8 Å), (3 GPa, 12.0 Å), (12 GPa, 10.8 Å), and (12 GPa, 13.4 Å) during the LLPT, suggesting that the atomic diffusivity in the x−y plane strengthens during the formation of a new layer. Actually, these peak points can be considered as the transition points of LLPTs. For instance, at $P_{\parallel}$ = 3 GPa, the system is in the state of the BIL at SS < 12.0 Å and to change into the TRIL when the slit size is larger than 12.0 Å. As shown in in Figure 4d, the average potential energy (E_{p}) also exhibits maxima at the transition points, suggesting the more unstable state during the LLPT than the layering state due to the strong atomic diffusion in the LLPT. As $P_{\parallel}$ increases, E_{p} tends to decrease, indicating that the system becomes more stable and more ordered under higher pressure.

The above discussions are mainly about the confinement-induced LLPT under constant pressure. Then, we investigate how the system changes with respect to the lateral pressure. As shown in Figure 5a, the distribution of coordinated structures during the BIL−TRIL transition is different from that induced by nanoconfinement. At $P_{\parallel}$ = 18 GPa, the number of central-Si TRIS reduces greatly, while the PENTAS of Si gradually becomes dominant since the high pressure increases the coordination of silicon atoms, leading to the replacement of TRIS by PENTAS and TETRAS. Compared to the TRIL at
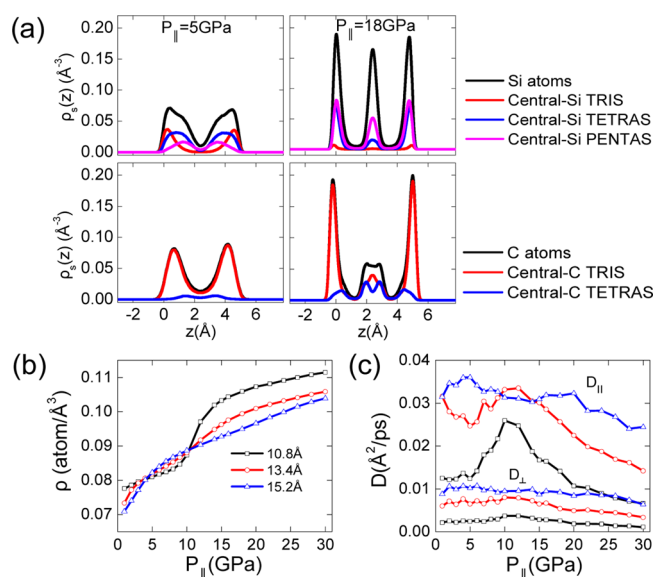
Figure 5. (a) Number density profiles $[\rho_s(z)]$ of different coordinated structures at SS = 10.8 Å. The system changes from bilayer to trilayer, over $P_{\parallel}$ = 5−18 GPa. (b) Density (ρ) of the system and (c) $D_{\parallel}$ and $D_{\perp}$ as a function of $P_{\parallel}$ for three different slit sizes: 10.8 Å (square), 13.4 Å (circle), and 15.2 Å (top triangle). In (c), the top three curves show the change of $D_{\parallel}$, and the bottom three curves show the change of $D_{\perp}$.

low pressure, there is a main peak with two shoulder peaks for the central-C TRIS in the middle layer at $P_{\parallel}$ = 18 GPa because the planar structure can tilt in an angle with walls. Two peaks for the central-C TETRAS are exhibited at the high pressure due to its nonplanar structure. Figure 5b presents an obvious abrupt density change at ($P_{\parallel}$, SS) = (12 GPa, 10.8 Å), which is the transition point of LLPTs, but the density at SS = 13.4 and 15.2 Å shows no significant change, revealing the weakening effect of the pressure at large slit sizes, which can also be confirmed by the diffusivity shown in Figure 5c, with a sharper peak at small SS. The $D_{\parallel}$ shows peaks at specific $P_{\parallel}$, which should be considered as the transition pressure of LLPTs, while the $D_{\perp}$ remains unchanged with respect to pressure. The decreasing slit size leads to the weakening of both $D_{\parallel}$ and $D_{\perp}$. Besides, $D_{\parallel}$ and $D_{\perp}$ remain the same order of magnitude over $P_{\parallel}$ = 1−30 GPa at different slit sizes, suggesting that this system maintains the liquid state at high pressure.

We also consider the effect of the LJ parameters between walls and particles. By keeping the LJ epsilon between walls and atoms of one component, we increased the LJ epsilon for the other component by 10-fold. Although the wall−liquid LJ potential strengthens, the LLPTs between different layering phases still exist with respect to the lateral pressure and slit sizes. Figure 6a,b presents the density profile of the system with different LJ epsilons at SS = 11.4 Å and $P_{\parallel}$ = 12 GPa. For the LJ epsilon of $10\varepsilon_{\mathrm{Si\text{-}wall}}$ and $\varepsilon_{\mathrm{C\text{-}wall}}$, the system is in the TRIL state and a separation between the silicon layer and the carbon layer adjacent to the walls occurs in the z direction, with carbon atoms close to the walls. However, when the LJ epsilon between carbon atoms and walls is set as $10\varepsilon_{\mathrm{C\text{-}wall}}$, silicon atoms are absorbed to walls more tightly than carbon atoms, which is reverse of the TRIL under normal LJ parameters. It can be deduced that the increase of LJ epsilons has a similar effect to the narrowing of slits, which is confirmed by the shift of the LLPT transition region to larger slit sizes when the LJ epsilon increases, as shown in Figure 6c. Notably, there are two peaks
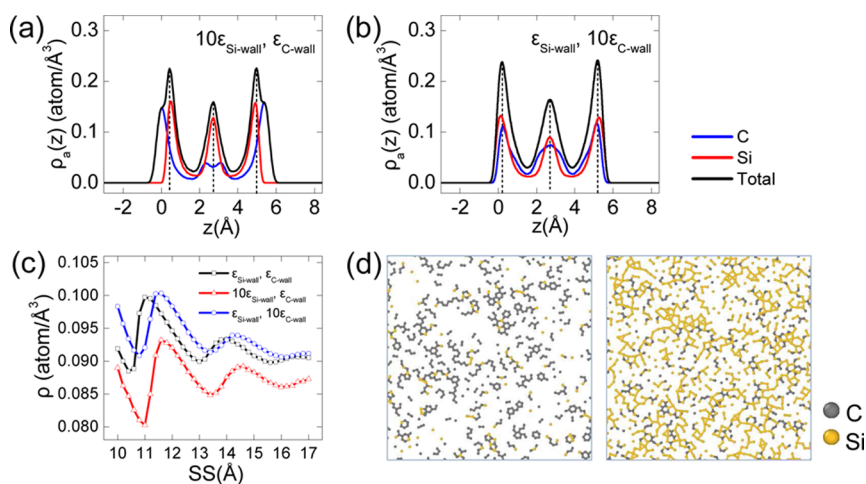
Figure 6. Density profiles [$\rho_a(z)$] for the LJ epsilon of (a) $10\varepsilon_{\text{Si-wall}}$, $\varepsilon_{\text{C-wall}}$, and (b) $\varepsilon_{\text{Si-wall}}$, $10\varepsilon_{\text{C-wall}}$, at SS = 11.4 Å and $P_{\parallel}$ = 12 GPa. (c) Density (ρ) change with different LJ epsilons at $P_{\parallel}$ = 12 GPa. (d) Layer separation of carbon atoms and silicon atoms in the system with $10\varepsilon_{\text{Si-wall}}$ and $\varepsilon_{\text{C-wall}}$. The left snapshot shows the configuration of the slab next to one of the walls (5.075 Å $\leq z \leq$ 6.225 Å); the right snapshot shows the configuration of the neighboring slab (3.675 Å $\leq z \leq$ 5.075 Å). At z = 5.075 Å, the density profiles of carbon atoms and silicon atoms show an intersection in the layer adjacent to walls shown in (a).

for carbon atoms in the middle layer at $10\varepsilon_{\text{Si-wall}}$ and $\varepsilon_{\text{C-wall}}$, indicating that the carbon tetralayer begins to form. Interestingly, when the LJ epsilon equals $10\varepsilon_{\text{Si-wall}}$ and $\varepsilon_{\text{C-wall}}$, the density decreases, while the system becomes denser at the LJ epsilon of $\varepsilon_{\text{Si-wall}}$ and $10\varepsilon_{\text{C-wall}}$. This might be because the strong wall−silicon force moves silicon atoms away from walls, leading to more carbon atoms close to the walls and increased volume. According to the layer separation presented in Figure 6a, the snapshots in the slab next to one of the walls (5.075 Å $\leq z \leq$ 6.225 Å) and in the neighboring slab (3.675 Å $\leq z \leq$ 5.075 Å) are shown in Figure 6d. Specifically, there is an intersection at z = 5.075 Å between the density profiles of carbon atoms and silicon atoms in Figure 6a. Due to the separation of the silicon layer and carbon layer, the local structure is exhibited clearly. Carbon atoms tend to form hexagonal strings and rings, while silicon atoms tend to show tetrahedral or distorted tetrahedral order.

Considering all of the above discussions, we plot the LLPT phase diagram of the confined liquid SiC with respect to $P_{\parallel}$ and SS under the normal LJ epsilon. As mentioned above, the transition points of LLPTs can be determined by the positions of the maxima of $D_{\parallel}$ and E_p. However, this method is not always effective. For instance, it is hard to find the second maximum point of $D_{\parallel}$ and E_p accurately in the $D_{\parallel}$−SS curve and the E_p−SS curve at $P_{\parallel}$ = 1 GPa in Figure 4c,d. Interestingly, the density and $P_{\perp}$ show the highest increase rates at these transition points, and we perform the derivatives of density and $P_{\perp}$ with respect to the slit size at a constant $P_{\parallel}$, as shown in Figure 7a,b. At $P_{\parallel}$ = 3 GPa, for instance, both $(\partial\rho/\partial\text{SS})_{P_{\parallel}}$ and $(\partial P_{\perp}/\partial\text{SS})_{P_{\parallel}}$ peak at SS = 12.0 and 15.0 Å, which are the transition points of the BIL−TRIL transition and the TRIL−TETRAL transition, respectively. Besides, the peaks in the $(\partial\rho/\partial\text{SS})_{P_{\parallel}}$−SS curve and the $(\partial P_{\perp}/\partial\text{SS})_{P_{\parallel}}$−SS curve seem to be sharper than those in the $D_{\parallel}$−SS curve and the E_p−SS curve, providing a more accurate approach to determine the transition points of LLPTs. The obtained transition points are denoted by open points in the ($P_{\parallel}$, SS) plane as shown in Figure 7c. By connecting these open points with smooth curves, we obtain the LLPT lines. Notably, in the LLPT lines, $(\partial P_{\perp}/\partial\text{SS})_{P_{\parallel}} < 0$.
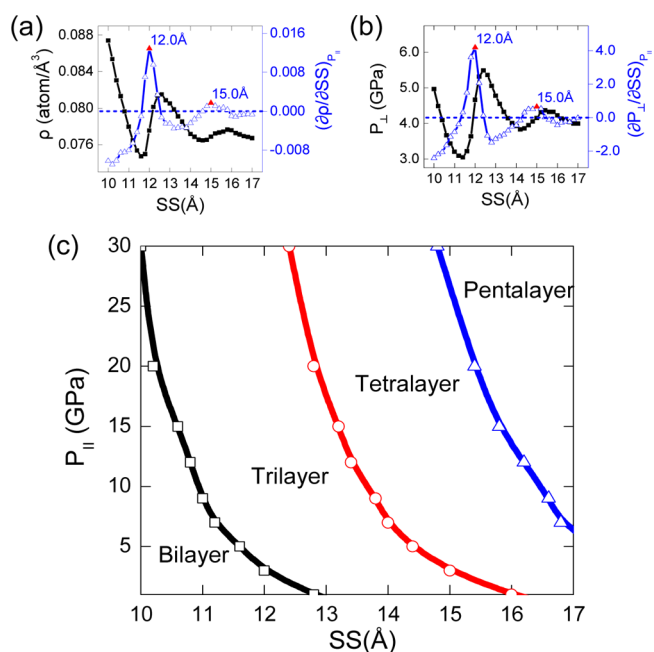
Figure 7. Phase diagram of the LLPT in the confined liquid SiC. (a) Density (ρ) and its derivatives with respect to the slit size, [$(\partial\rho/\partial\text{SS})_{P_{\parallel}}$]. (b) $P_{\perp}$ and its derivatives with respect to the slit size, [$(\partial P_{\perp}/\partial\text{SS})_{P_{\parallel}}$], as a function of the slit size at $P_{\parallel}$ = 3 GPa. (c) $P_{\parallel}$−SS phase diagram at normal LJ parameters. The open point representing the transition point in (c) is determined by the maxima of $(\partial\rho/\partial\text{SS})_{P_{\parallel}}$ and $(\partial P_{\perp}/\partial\text{SS})_{P_{\parallel}}$ (red triangles) in (a) and (b). For instance, at $P_{\parallel}$ = 3 GPa, $(\partial\rho/\partial\text{SS})_{P_{\parallel}}$ and $(\partial P_{\perp}/\partial\text{SS})_{P_{\parallel}}$ both reach the maximum at SS = 12.0 Å, which is the transition point between the bilayer liquid and the trilayer liquid.

Besides, the absolute value |$\partial P_{\parallel}/\partial\text{SS}$| at higher $P_{\parallel}$ is larger than that at lower $P_{\parallel}$. This means that, under high pressure, the LLPT is mainly induced by the slit size, but under low pressure, it is dominantly induced by pressure.

CONCLUSION

In conclusion, we carried out MD simulations on the evidence of an LLPT in the nanoconfined liquid SiC. We consider that the layering transition characterized by the rapid change of density is actually a type of LLPT. The space distribution change of the TRIS, TETRAS, and PENTAS is found to be responsible for the internal mechanism of the LLPT. Silicon has the dominant structure of TRIS, TETRAS, and PENTAS, while carbon is mainly determined by the TRIS. The central-C TRIS tends to form a planar structure, exhibiting the sp^2 characteristic, while the structure of central-Si TRIS is a quadrihedron, causing the microphase separation between carbon atoms and silicon atoms in the layer adjacent to walls. The strong wall−silicon force leads to the layer separation between silicon and carbon. Specifically, the pressure confinement phase diagram is plotted with negative slopes for the LLPT lines. The different slope value of LLPT lines at different pressure suggests a confinement-induced LLPT at high pressure and a pressure-induced LLPT at low pressure. Our results strongly indicate a different behavior of LLPTs between the heterogeneous liquid and the homogeneous liquid.

AUTHOR INFORMATION

Corresponding Author

*lihuilmy@hotmail.com

Notes

The authors declare no competing financial interest.

ACKNOWLEDGMENTS

REFERENCES

(1) Mishima, O.; Calvert, L.; Whalley, E. *Nature* **1984**, *310*, 393.

(2) Mishima, O.; Calvert, L.; Whalley, E. *Nature* **1985**, *314*, 76.

(3) Deb, S. K.; Wilding, M.; Somayazulu, M.; McMillan, P. F. *Nature* **2001**, *414*, 528.

(4) McMillan, P. F.; Wilson, M.; Daisenberger, D.; Machon, D. *Nat. Mater.* **2005**, *4*, 680.

(5) Daisenberger, D.; Wilson, M.; McMillan, P. F.; Cabrera, R. Q.; Wilding, M. C.; Machon, D. *Phys. Rev. B: Condens. Matter Mater. Phys.* **2007**, *75*, 224118.

(6) Daisenberger, D.; Deschamps, T.; Champagnon, B.; Mezouar, M.; Quesada Cabrera, R. l.; Wilson, M.; McMillan, P. F. *J. Phys. Chem. B* **2011**, *115*, 14246.

(7) Aptekar, L. *Phys.-Dokl.* **1979**, *24*, 993.

(8) Sastry, S.; Angell, C. A. *Nat. Mater.* **2003**, *2*, 739.

(9) Jakse, N.; Pasturel, A. *Phys. Rev. Lett.* **2007**, *99*, 205702.

(10) Ganesh, P.; Widom, M. *Phys. Rev. Lett.* **2009**, *102*, 075701.

(11) Beye, M.; Sorgenfrei, F.; Schlotter, W. F.; Wurth, W.; Föhlisch, A. *Proc. Natl. Acad. Sci. U. S. A.* **2010**, *107*, 16772.

(12) Zhang, K.; Li, H.; Jiang, Y. *Phys. Chem. Chem. Phys.* **2014**, *16*, 18023.

(13) Zhao, G.; Yu, Y.; Tan, X. *J. Chem. Phys.* **2015**, *143*, 054508.

(14) Okada, J.; Sit, P.-L.; Watanabe, Y.; Wang, Y.; Barbiellini, B.; Ishikawa, T.; Itou, M.; Sakurai, Y.; Bansil, A.; Ishikawa, R.; et al. *Phys. Rev. Lett.* **2012**, *108*, 067402.

(15) Tanaka, H. *Phys. Rev. B: Condens. Matter Mater. Phys.* **2002**, *66*, 064202.

(16) Morishita, T. *Phys. Rev. Lett.* **2006**, *97*, 165502.

(17) Wang, Y.; Zhao, G.; Liu, C.; Zhu, Z. *Phys. B* **2011**, *406*, 3991.

(18) Miranda, C. R.; Antonelli, A. *J. Chem. Phys.* **2004**, *120*, 11672.

(19) Ganesh, P.; Widom, M. *J. Non-Cryst. Solids* **2011**, *357*, 442.

(20) Vasisht, V. V.; Saw, S.; Sastry, S. *Nat. Phys.* **2011**, *7*, 549.

(21) Morishita, T. *Phys. Rev. E* **2005**, *72*, 021201.

(22) Jakse, N.; Pasturel, A. *J. Chem. Phys.* **2008**, *129*, 104503.

(23) Cajahuaringa, S.; de Koning, M.; Antonelli, A. *J. Chem. Phys.* **2013**, *139*, 224504.

(24) Ferraz, A.; March, N. *Phys. Chem. Liq.* **1979**, *8*, 289.

(25) Van Thiel, M.; Ree, F. *Phys. Rev. B: Condens. Matter Mater. Phys.* **1993**, *48*, 3591.

(26) van Thiel, M.; Ree, F. H. *J. Appl. Phys.* **1995**, *77*, 4804.

(27) Togaya, M. *Phys. Rev. Lett.* **1997**, *79*, 2474.

(28) Glosli, J. N.; Ree, F. H. *Phys. Rev. Lett.* **1999**, *82*, 4659.

(29) Ghiringhelli, L. M.; Los, J. H.; Meijer, E. J.; Fasolino, A.; Frenkel, D. *Phys. Rev. B: Condens. Matter Mater. Phys.* **2004**, *69*, 100101.

(30) Johnson, S.; Heimann, P.; MacPhee, A.; Lindenberg, A.; Monteiro, O.; Chang, Z.; Lee, R.; Falcone, R. *Phys. Rev. Lett.* **2005**, *94*, 057407.

(31) He, Y.; Li, H.; Jiang, Y.; Li, X.; Bian, X. *Sci. Rep.* **2014**, *4*, 3635.

(32) Wu, C. J.; Glosli, J. N.; Galli, G.; Ree, F. H. *Phys. Rev. Lett.* **2002**, *89*, 135701.

(33) Kum, O.; Ree, F. H.; Stuart, S. J.; Wu, C. J. *J. Chem. Phys.* **2003**, *119*, 6053.

(34) Ghiringhelli, L. M.; Los, J. H.; Meijer, E. J.; Fasolino, A.; Frenkel, D. *Phys. Rev. Lett.* **2005**, *94*, 145701.

(35) Morris, J.; Wang, C.; Ho, K. *Phys. Rev. B: Condens. Matter Mater. Phys.* **1995**, *52*, 4138.

(36) Correa, A. A.; Bonev, S. A.; Galli, G. *Proc. Natl. Acad. Sci. U. S. A.* **2006**, *103*, 1204.

(37) Eggert, J.; Hicks, D.; Celliers, P.; Bradley, D.; McWilliams, R.; Jeanloz, R.; Miller, J.; Boehly, T.; Collins, G. *Nat. Phys.* **2010**, *6*, 40.

(38) Ghiringhelli, L. M.; Los, J. H.; Meijer, E. J.; Fasolino, A.; Frenkel, D. *J. Phys.: Condens. Matter* **2005**, *17*, S3619.

(39) Wang, X.; Scandolo, S.; Car, R. *Phys. Rev. Lett.* **2005**, *95*, 185701.

(40) Mélinon, P.; Masenelli, B.; Tournus, F.; Perez, A. *Nat. Mater.* **2007**, *6*, 479.

(41) Lin, X.; Lin, S.; Xu, Y.; Chen, H. *J. Mater. Chem. C* **2015**, *3*, 9057.

(42) Shi, Z.; Zhang, Z.; Kutana, A.; Yakobson, B. I. *ACS Nano* **2015**, *9*, 9802.

(43) Lin, S. *J. Phys. Chem. C* **2012**, *116*, 3951.

(44) Liu, D.; Zhang, Y.; Chen, C.-C.; Mou, C.-Y.; Poole, P. H.; Chen, S.-H. *Proc. Natl. Acad. Sci. U. S. A.* **2007**, *104*, 9570.

(45) Wu, W.; Zhang, L.; Ren, H.; Zhang, K.; Li, H.; He, Y. *Phys. Chem. Chem. Phys.* **2015**, *17*, 13380.

(46) He, Y.; Li, H.; Sui, Y.; Qi, J.; Wang, Y.; Chen, Z.; Dong, J.; Li, X. *Sci. Rep.* **2015**, *5*, 14792.

(47) Liu, Q.; Zou, R.; Bando, Y.; Golberg, D.; Hu, J. *Prog. Mater. Sci.* **2015**, *70*, 1.

(48) Soldano, C. *Prog. Mater. Sci.* **2015**, *69*, 183.

(49) Li, Y.; Wu, X.; Wu, Q.; Ding, H.; Yan, W. *Ind. Eng. Chem. Res.* **2014**, *53*, 12920.

(50) Huang, T.; Tian, N.; Wu, Q.; Yan, W. *Soft Matter* **2015**, *11*, 4481.

(51) Plimpton, S. *J. Comput. Phys.* **1995**, *117*, 1.

(52) Tersoff, J. *Phys. Rev. B: Condens. Matter Mater. Phys.* **1989**, *39*, 5566.

(53) Shen, H. *J. Mater. Sci.* **2007**, *42*, 6382.

(54) Zhou, R.; Wang, L.; Pan, B. *J. Phys. Chem. C* **2010**, *114*, 8199.

(55) Stuart, S. J.; Tutein, A. B.; Harrison, J. A. *J. Chem. Phys.* **2000**, *112*, 6472.

(56) Qiu, B.; Wang, Y.; Zhao, Q.; Ruan, X. *Appl. Phys. Lett.* **2012**, *100*, 233105.

(57) He, Y.; Li, X.; Li, H.; Jiang, Y.; Bian, X. *Nanoscale* **2014**, *6*, 4217.

(58) Clark, S. J.; Segall, M. D.; Pickard, C. J.; Hasnip, P. J.; Probert, M. I.; Refson, K.; Payne, M. C. *Z. Kristallogr. - Cryst. Mater.* **2005**, *220*, 567.

(59) Wilson, M.; McMillan, P. F. *Phys. Rev. Lett.* **2003**, *90*, 135703.

(60) Chehaidar, A.; Carles, R.; Zwick, A.; Meunier, C.; Cros, B.; Durand, J. *J. Non-Cryst. Solids* **1994**, *169*, 37.

(61) Aasland, S.; McMillan, P. *Nature* **1994**, *369*, 633.